Acta Materialia 203 (2021) 116487

Contents lists available at ScienceDirect

Acta Materialia

journal homepage: www.elsevier.com/locate/actamat

Chemical and structural origin of hole states in yttria-stabilized zirconia

Yanhao Dong[a], Yimeng Huang[b], Dong Ding[c], Wei Wu[c], Xiahui Yao[a], Ju Li[a,b,*]

[a] Department of Nuclear Science and Engineering, Massachusetts Institute of Technology, Cambridge, MA, 02139, USA
[b] Department of Materials Science and Engineering, Massachusetts Institute of Technology, 77 Massachusetts Avenue, Cambridge, MA, 02139, USA
[c] Energy & Environmental Science and Technology, Idaho National Laboratory, Idaho Falls, ID 83415, USA

ARTICLE INFO

Article history:
Received 31 August 2020
Revised 7 November 2020
Accepted 10 November 2020
Available online 13 November 2020

Keywords:
Solid oxide fuel/electrolyzer cells
solid electrolyte
zirconia
p-type conductivity
anion redox

ABSTRACT

Yttria-stabilized zirconia (YSZ) has important electrochemical applications as a fast oxygen ion conductor and is the state-of-the-art electrolyte material for solid oxide fuel/electrolyzer cells. While much attention has been paid to the fast oxygen ion conduction, the electronic conductivity and especially hole carriers are not well understood, yet essential for the electrochemical stability, conduction kinetics and microstructural evolution in YSZ. The present work uses first-principles calculations to illustrate the chemical nature and local structural features of hole states in oxidized YSZ. Three types of hole states have been identified, including delocalized hole states on normal oxygen ions, localized hole states on special oxygen ions with extreme local structures, and peroxide-like groups. The implications on various experimental observations are discussed.

1. Introduction

Yttria stabilized zirconia (YSZ) is an important ceramic material, and it is widely used as a structural ceramic, thermal barrier coating, and as the electrolyte in oxygen sensors and solid oxide fuel/electrolyzer cells (SOFC/SOEC). [1-3] For electrochemical applications, cubic YSZ (e.g., 8 mol% yttria-stabilized zirconia with chemical formula $Y_{0.148}Zr_{0.852}O_{1.926}$, abbreviated as 8YSZ) is well known for its high oxygen ion conductivity $\sigma_{O^{2-}}$ at elevated temperatures, which combined with a large band gap, low electronic conductivity (including both electron conductivity σ_e and hole conductivity σ_h) [4-6] and a stable microstructure (minimum grain growth <1200°C, due to slow cation diffusion) [7-9] makes it a popular solid electrolyte for SOFC/SOEC operated at 600-1000°C. Its predominant ionic conduction is illustrated by the conductivity data (at 800°C) [4] in Fig. 1a, where $\sigma_{O^{2-}}$ is >1,000 times higher than σ_e and σ_h over a wide range of oxygen potential $\mu_{O_2} \equiv \mu_{O_2}^{\ominus} + k_B T \ln PO_2$ (i.e., the chemical potential of oxygen, with k_B being the Boltzmann constant, T the absolute temperature, PO_2 the oxygen partial pressure, and $\mu_{O_2}^{\ominus}$ the oxygen potential set as 0 eV at the standard state condition of PO_2=1 atm) from −5 eV (corresponding to $PO_2=3.27 \times 10^{-24}$ atm) to 1 eV (corresponding to $PO_2=4.98 \times 10^{4}$ atm). While the celebrated O^{2-} conduction has been extensively studied over decades by various experimental and simulation techniques [4,10-12], the electronic conductivity and the minority charge carriers of electrons and holes have received much less attention in YSZ and in many other solid electrolytes. Nevertheless, the significance of the minority electronic current and electronic defects has recently been highlighted as critical for understanding (i) chemical equilibrium and degradations of solid-electrolyte-based devices (e.g., oxygen bubble formation inside solid electrolytes under SOEC operations) [13-20], (ii) enhanced conductivity and transition from p-type to n-type behavior under voltage bias and non-equilibrium conditions [21-23], and (iii) enhanced mass transport and microstructural evolution during field-assisted processing [24-27] (e.g., flash sintering [27]).

In YSZ, Y^{3+} substitutions on Zr^{4+} sites are charge-compensated by doubly charged oxygen vacancies, which using Kröger-Vink notation can be written as

$$Y_2O_3 = 2Y'_{Zr} + V_O^{\bullet\bullet} + 3O_O^{\times} \quad (1)$$

Because of the heavy doping and large enthalpy penalties to reduce/oxidize YSZ, the concentration of $V_O^{\bullet\bullet}$ is extrinsically fixed and $\sigma_{O^{2-}}$ remains constant over a large μ_{O_2} range as shown in Fig. 1a, thus setting a large electrolytic window for YSZ electrolytes. While very limited under most μ_{O_2}, reduction of YSZ can still take place by creating extra $V_O^{\bullet\bullet}$ and electrons

$$O_O^{\times} = V_O^{\bullet\bullet} + 2e + 1/2O_2 \quad (2)$$

* Corresponding author.
E-mail address: liju@mit.edu (J. Li).

https://doi.org/10.1016/j.actamat.2020.116487
1359-6454/

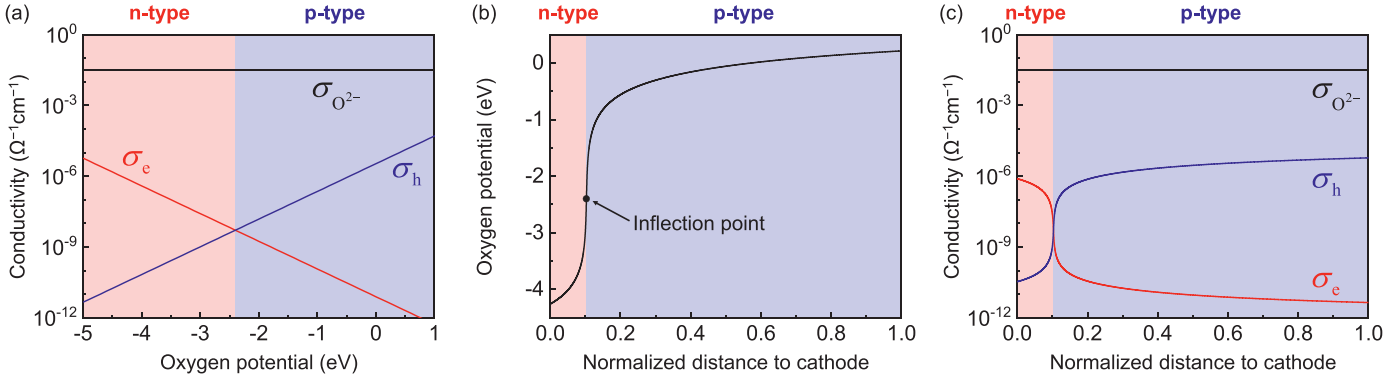

Fig. 1. (a) Conductivity data of 8YSZ at 800°C. Spatial distributions of (b) μ_{O_2}, (c)$\sigma_{O^{2-}}$, σ_e, and σ_h inside a 10 μm YSZ electrolyte operated in SOEC mode under −1 A/cm^2 at 800°C, with $\mu'_{O_2} = -4.26$eV at cathode/electrolyte interface and $\mu''_{O_2} = 0.21$eV at anode/electrolyte interface. Shaded regions in red and blue denote the n- and p-type characteristics of the minor electronic conductivity, respectively.

and oxidation can take place by filling in $V_O^{\bullet\bullet}$ and creating holes

$$V_O^{\bullet\bullet} + 1/2O_2 = O_O^{\times} + 2h \tag{3}$$

Following defect chemical analysis, the above reduction and oxidation reactions can be shown to create minority electron and hole conductivities give by $\sigma_e \propto \exp(-\mu_{O_2}/4k_BT) \propto PO_2^{-1/4}$ and $\sigma_h \propto \exp(\mu_{O_2}/4k_BT) \propto PO_2^{+1/4}$ in Fig. 1a, provided the mobilities of electrons and holes are PO_2-independent [4]. Therefore, in μ_{O_2} space, the electron/hole contribution to the electronic conductivity $\sigma_{eh} = \sigma_e + \sigma_h$ defines an n-type region under more reducing conditions where $\sigma_e > \sigma_h$, a p-type region under more oxidizing conditions where $\sigma_e < \sigma_h$, and a p-n transition at an intermediate μ_{O_2} where $\sigma_e = \sigma_h$. Such dependencies and V-shape σ_{eh} translate to a sharp p-n transition in real space, as YSZ electrolytes are typically sandwiched between a highly reducing atmosphere at one electrode and a highly oxidizing one at the other electrode (e.g., fuel gas and air in SOFC/SOEC), so that the steepest μ_{O_2} drop occurs at the electronic conductivity minimum $(\sigma_{eh})_{min}$ to maintain a spatially uniform electronic current. (If the electronic current $\mathbf{J}_{eh}(\mathbf{x})$ is not uniform in 1D or divergence-free in 3D, there will be a net redox reaction at that location, e.g., $2O^{2-} \rightarrow O_2(g) + 4e$, and then the concentrations of ionic/neutral species cannot be at steady-state, the assumption in most situations.) One such example is shown in Fig. 1b-c, where the spatial distributions of μ_{O_2}, $\sigma_{O^{2-}}$, σ_e, and σ_h inside a 10 μm thick YSZ membrane were calculated for a SOEC operated under −1 A/cm^2 at 800°C, with $\mu'_{O_2} = -4.26$eV (corresponding to PO_2=10^{-20} atm) at the cathode/electrolyte interface and $\mu''_{O_2} = 0.21$eV (corresponding to PO_2=10 atm) at the anode/electrolyte interface [15]. Such a sharp p-n transition in real space has profound implications in practical applications: For example, in flash sintering, the dynamic conversion between electrons and holes at the p-n transition is proposed to be responsible for the observed electroluminescence [23,28]; in electric field-assisted superplasticity of tetragonal zirconia [29], the mass transport and grain boundary sliding can be enhanced in the n-type region but not in the p-type region [24-26], thus leading to final fracture at the p-n transition; in solid electrolyte-based devices such as SOFC/SOEC and all-solid-state batteries, the sharp p-n transition sets a step-like chemical potential profile for the corresponding neutral species (e.g., O_2 for SOFC/SOEC and Li for lithium-ion batteries), thus subjecting the electrolyte to be influenced by the electrode overpotentials that can drive degradation [16]. Therefore, holes constitute a significant part of the electronic conduction both in μ_{O_2} and in real space, and complete understandings of the electronic disorder as well as the associated p-n transition are critical to the various problems in materials processing and service. However, while the nature of electron states in reduced zirconia has been investigated and discussed in the literature [30-32], little attention was paid to the chemical nature of hole states and mobility mechanisms. This sets the background of the present work, which seeks to use first-principles calculations to understand the chemistry of anion redox and local structural features for oxygen hole states in YSZ at an atomistic level.

Outside YSZ and solid electrolytes, there are many investigations concerned with anion-redox processes in battery electrodes, especially in the so-called lithium-excess cathode materials for lithium-ion batteries [33-36]. These are lithium-containing transition-metal oxides that can be delithiated/lithiated reversibly at high voltages and the available transition-metal redox capacity is insufficient to fully compensate the charge of lithium removal so that oxygen redox reactions also participate. It turns out that the redox-active oxygen states come from extreme local structures, which decrease the number of coordinating transition metal ions around some oxygen in a rock-salt structure framework thus creating less hybridized and higher-energy oxygen 2p states on top of the broad oxygen 2p band [35,36]. It leads to localized hole states on oxygen upon oxidation, producing oxidized oxygen ion $O^{\alpha-}$ instead of the "standard" O^{2-} anion. Note here that $0<\alpha<2$ and it is not necessarily an integer. Nevertheless, if one sticks to integer valences for simplicity, the oxidized oxygen ion can be treated as O^-. This inspires us to study the correlation between local structures and the electronic density of states (DOS) for oxygen ions in YSZ. As shall be described, three types of hole states—(i) delocalized hole states on oxygen ion O^{2-}, (ii) localized hole states on oxygen $O^{\alpha-}$ or $(O_2)^{3-}$ complex with α=1.5, and (iii) peroxide-group-like $(O_2)^{2-}$ with α=1, all with distinct local structural features—have been identified in oxidized YSZ. The implications of the identified hole states shall be discussed.

2. Methods

Spin-polarized first-principles calculations were conducted using the Vienna *ab initio* simulation package (VASP) based on density functional theory (DFT) following the projector augmented-wave (PAW) method under Perdew-Burke-Ernzerhof (PBE) generalized gradient approximation (GGA). [37-39] PAW potentials including $4s^24p^65s^24d^2$ electrons for Zr, $4s^24p^65s^24d^1$ electrons for Y, and $2s^22p^4$ electrons for O and a plane-wave cutoff energy of 400 eV were used. For 0 K calculations, the convergence was considered to be reached when the residual atomic forces were <0.05 eV/Å. To simulate cubic YSZ, we first built a 2 × 2 × 2 supercell for cubic ZrO_2 (containing 32 Zr and 64 O), then randomly substituted six Zr with six Y and removed three O (i.e., creating three oxygen vacancies $V_O^{\bullet\bullet}$). This created a $Zr_{26}Y_6O_{61}$ super-

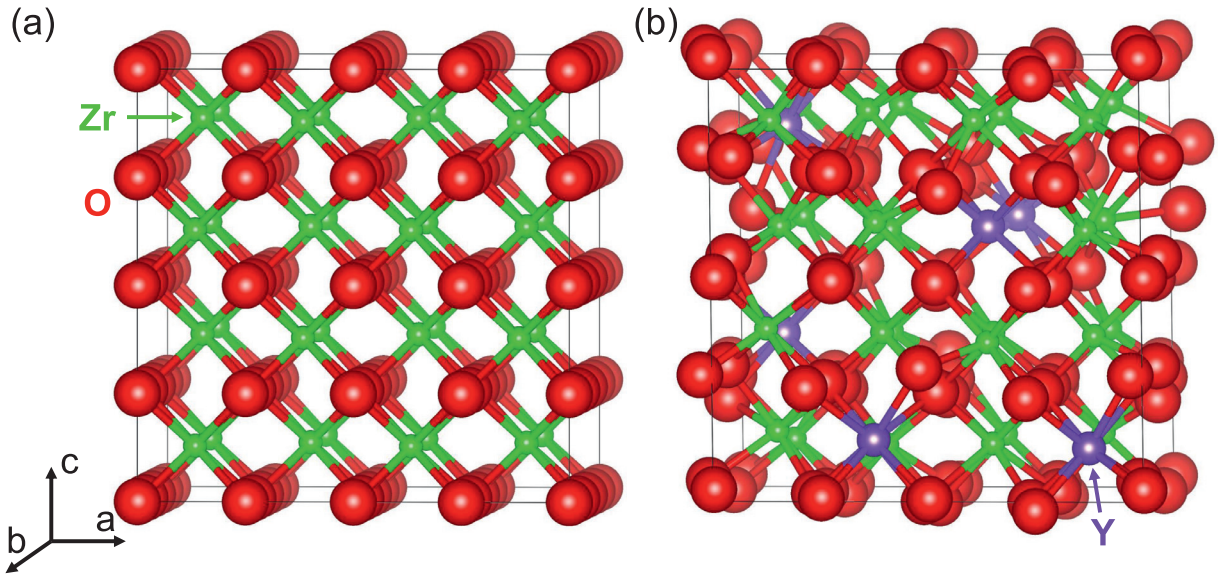

Fig. 2. Atomic structures of (a) cubic ZrO_2 and (b) cubic YSZ. Zr in green, Y in purple and O in red.

cell with a composition of $Y_{0.188}Zr_{0.813}O_{1.906}$ close to that of 8YSZ. Since there are strong $Y/Zr - V_O^{\bullet\bullet}$ interactions and the distribution of $V_O^{\bullet\bullet}$ is not random ($V_O^{\bullet\bullet}$ prefers to be the first nearest neighbor of Zr^{4+} [40] and the second nearest neighbor of Y^{3+} [12,41]), to achieve more "realistic" configurations in a consistent manner, we conducted first-principles molecular dynamics calculations to anneal the as-built atomic structures at high temperatures (at 1200 K, 900 K, 600 K and 300 K, each for 1.5 ps) and then relaxed the structures at 0 K. Such a treatment tries to mimic the behavior that in real YSZ samples, the sluggish cation diffusion renders the quasi-random Zr/Y distribution in the bulk, while the oxygen ion and $V_O^{\bullet\bullet}$ are allowed to relax their spatial distributions at a faster time scale. To simulate oxidized cubic YSZ, using the annealed and relaxed YSZ supercell, we either (i) filled in one $V_O^{\bullet\bullet}$ by a neutral oxygen atom to build a $Zr_{26}Y_6O_{62}$ supercell, or (ii) filled in two $V_O^{\bullet\bullet}$ by two neutral oxygen atoms to build a $Zr_{26}Y_6O_{63}$ supercell. Note (i-ii) follow oxidation reaction Eq. (3) and the supercells are charge-neutral. The as-built supercells for oxidized cubic YSZ were similarly annealed by first-principles molecular dynamics calculations (at 1200 K, 900 K, 600 K and 300 K, each for 1.5 ps), followed by 0 K relaxation. The above procedures were repeated for three times to obtain three sets of individually simulated results in the $Zr_{26}Y_6O_{61}$ supercell for the reference un-oxidized cubic YSZ and in the $Zr_{26}Y_6O_{62}$ and $Zr_{26}Y_6O_{63}$ supercells for the oxidized cubic YSZ. Throughout the study, the Brillouin zone was sampled using Monhorst-Pack scheme with a $3 \times 3 \times 3$ **k**-point mesh for 0 K calculations and with a $1 \times 1 \times 1$ **k**-point mesh for first-principles molecular dynamics calculations. The atomic structures and charge density distributions were visualized and plotted using software VESTA [42].

3. Results

Cubic ZrO_2 (Fig. 2a) has a fluorite structure with space group $Fm\bar{3}m$. In the perfect structure, simple-cubic-packed oxygen ions all have the same local structure, occupying the tetrahedral site surrounded by four coordinating Zr cations, while the Zr cations occupy half of the cubes formed by eight coordinating O anions. In comparison, the atomic structure of cubic YSZ is quite defective (Fig. 2b), with distortions at all lattice sites due to the large concentrations of Y'_{Zr} and $V_O^{\bullet\bullet}$. This breaks down the cubic symmetry in the local structure and creates various local environments for different Y, Zr and O, even though a "global" cubic symmetry can still be observed by diffraction techniques on a larger length scale. The fluctuations in local structures also result in localized hole states in oxidized YSZ, as shall be discussed. Regarding the electronic structure, as shown by the density of states (DOS) in Fig. 3a, cubic YSZ (simulated by a $Zr_{26}Y_6O_{61}$ supercell) has a valence band composed mainly of O 2*p* orbitals (hybridized with Zr/Y 4*d* orbitals), a conduction band composed mainly of Zr/Y 4*d* orbitals (hybridized with O 2*p* orbitals), and a well-defined bandgap without any gap states. There is no net magnetic moment for the simulated $Zr_{26}Y_6O_{61}$ supercell, as also can be seen from the symmetric spin-up (positive) and spin-down (negative) states in the DOS in Fig. 3a.

We next simulated an oxidized cubic YSZ with a $Zr_{26}Y_6O_{62}$ supercell by adding one neutral O atom (i.e., adding one O^{2-} and two holes) to the reference $Zr_{26}Y_6O_{61}$ supercell, followed by annealing and relaxation as described in **Section II**. As shown by DOS in Fig. 3b, while there are only minor changes in the valence band and conduction band, two unoccupied gap states emerge on top of the valence band maximum (VBM), and their peak positions lie at E_1=0.22 eV and E_2=0.69 eV above the Fermi level E_F (set as 0 eV). Note both states have little dispersion in energy and are mainly contributed by oxygen 2*p* orbitals, suggesting they are probably two localized hole states on oxygen with minimal hybridization with the cations. To figure out what the "oxidized" oxygen ions with localized hole states are, we calculated the Bader charges [43] for all the oxygen ions in the $Zr_{26}Y_6O_{62}$ supercell. (Bader charge analysis uses 2D zero-flux surface of valence electron density $\rho(\mathbf{x})$ to divide atoms, where $\rho(\mathbf{x})$ reaches minimum perpendicular to the surface, $\mathbf{n}(\mathbf{x})\bullet\nabla\rho(\mathbf{x})=0$. The charge enclosed within the dividing surfaces is called Bader charge, which is typically used to approximate the total electronic charge of an atom in atomistic calculations.) While most oxygen ions (58 out of 62) have Bader charges of $7.31\pm0.02e$ similar to the ones in the reference unoxidized YSZ ($7.31\pm0.03e$ for 61 O in the $Zr_{26}Y_6O_{61}$ supercell) and such "normal" oxygen ions can be treated as O^{2-}, we note four "special" oxygen ions with less Bader charges of $7.04\pm0.06e$, indicating localized hole states on them. We also noted that "normal" O^{2-} occupies the tetrahedral site with four coordinating cations (inset of Fig. 4a) and have no DOS (Fig. 4a) within the band gap

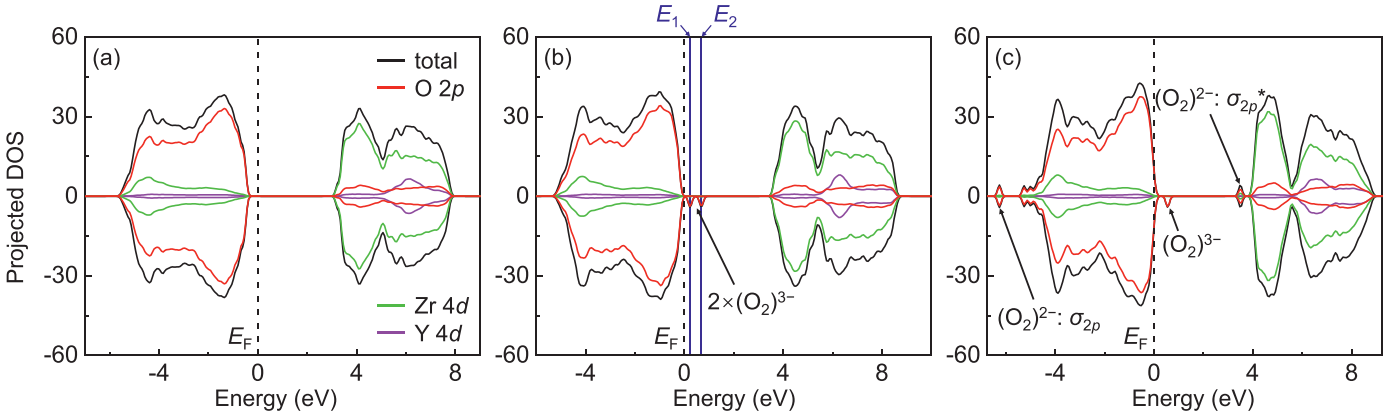

Fig. 3. Calculated total DOS, and projected DOS for O 2*p*, Zr 4*d*, and Y 4*d* orbitals for (a) a $Zr_{26}Y_6O_{61}$ supercell, (b) a $Zr_{26}Y_6O_{62}$ supercell, and (c) a $Zr_{26}Y_6O_{63}$ supercell. For *y*-axis, positive values denote spin-up states and negative values denote spin-down states. For *x*-axis, E_F is set as 0 eV.

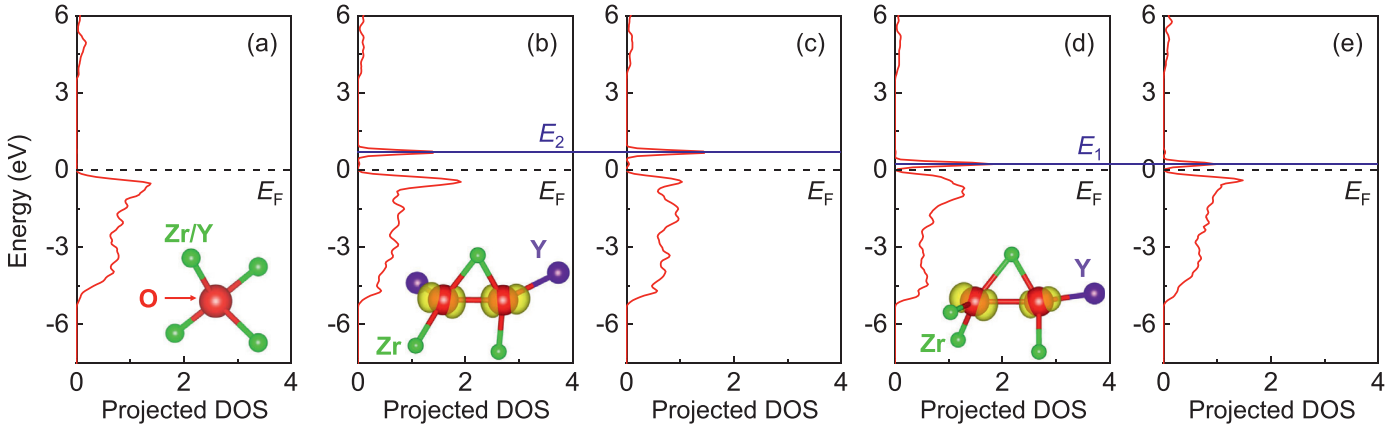

Fig. 4. Projected DOS of (a) O^{2-}, and (b-d) four "special" O in a $Zr_{26}Y_6O_{62}$ supercell. Inset of (a): local structure of O^{2-}. Inset of (b): local structures of two "special" O whose projected DOS is shown in (b-c). Inset of (d): local structures of two "special" O whose projected DOS is shown in (d-e). The iso-charge-density-surface drawn in insets of (b) and (d) is set as 0.01 *e*/Bohr^3 within the energy range of 0.0-1.0 eV vs. E_F.

between 0 eV and ~3.4 eV. In contrast, the four special oxygen ions have distinct features in their local structures and DOS: They are displaced further away from their lattice sites (tetrahedral site formed by four cations) and sit in the center of the triangle formed by three coordinating cations (insets of Fig. 4b and 4d), where the triangular planar configuration is enabled by an $V_O^{\bullet\bullet}$ in the neighboring tetrahedral site. The severe displacement is clearly shown by the appearance of a special oxygen ion in the two-dimensional (2D) slice of charge density distribution for a (100) plane cutting across the cation layer (Fig. 5a), while other (100) planes typically cut thought cations only (Fig. 5b). Meanwhile, the four special oxygen ions form two coordinating O-O pairs: The two oxygen ions plotted in the inset of Fig. 4b have an O-O bond length of 2.17 Å, Bader charges of 7.03*e* and 7.06*e*, and unoccupied projected DOS peaked at E_2; the two oxygen ions plotted in the inset of Fig. 4d have an O-O bond length of 2.41 Å, Bader charges of 6.97*e* and 7.12*e*, and unoccupied projected DOS peaked at E_1. We further confirmed these are indeed the localized hole states on oxygen by plotting band decomposed charge densities within the respective energy ranges, which are shown by the dumbbell-shape iso-charge-density-surfaces (in yellow) around the four oxygen ions in the insets of Fig. 4b (the gap state peaked at E_2) and Fig. 4d (the gap state peaked at E_1). Therefore, the four special oxygen ions are oxidized oxygen ion $O^{\alpha-}$ with localized hole states, and because a hole state is shared by a coordinating O-O pair, they can be referred as an $(O_2)^{3-}$ complex, with "oxidation progress variable" α=1.5. (Since an $V_O^{\bullet\bullet}$ is involved, it can also be expressed as a $(O_O^{\bullet}\cdot O_O^{\times}\cdot V_O^{\bullet\bullet})$ complex using Kröger-Vink notation. It also clearly differs from conventional peroxide group $(O_2)^{2-}$ and superoxide group $(O_2)^{-}$ in terms of atomic and electronic structures.) It is well-known that Bader charge analysis from DFT gives ionic charges less than the Kröger-Vink style formal charges. For example, for the standard O^{2-}, the Bader charge analysis gives $7.31e - 6e = 1.31e$, a factor of 1.53× from its formal charge of α=2. Thus, a Bader charge assignment $7.04e - 6e = 1.04e$ should not be taken to mean peroxide (α=1), but rather, if multiplying the same factor 1.53×, would be 1.59*e* after correction, and close to the α=1.5 formal assignment we have given above for the $(O_2)^{3-}$ complex. One can also interpret the $(O_2)^{3-}$ complex as oscillating between two resonant states in $(O_O^{\bullet}\cdot O_O^{\times}\cdot V_O^{\bullet\bullet})$. Finally, as one $(O_2)^{3-}$ has an unpaired electron, it creates a magnetic moment of 1 μ_B. Accordingly, the simulated $Zr_{26}Y_6O_{62}$ supercell containing 2 × $(O_2)^{3-}$ complexes would have a net magnetic moment of 2 μ_B, which we confirmed in our first-principles calculations.

We then considered further oxidation of cubic YSZ and simulated a $Zr_{26}Y_6O_{63}$ supercell by adding two neutral O atoms (i.e., adding two O^{2-} and four holes) to the reference $Zr_{26}Y_6O_{61}$ supercell, followed by the same annealing-relaxation process. Three distinct features are shown by DOS in Fig. 3c: (i) The Fermi level E_F enters the valence band and lies at ~0.23 eV below the VBM. The unoccupied DOS between E_F and VBM is mainly contributed by O 2*p* orbitals and has slightly more spin-down states than spin-up ones. (ii) There is a spin-down gap state above VBM at 0.54 eV (vs. E_F), with similar characteristics to the gap states identified

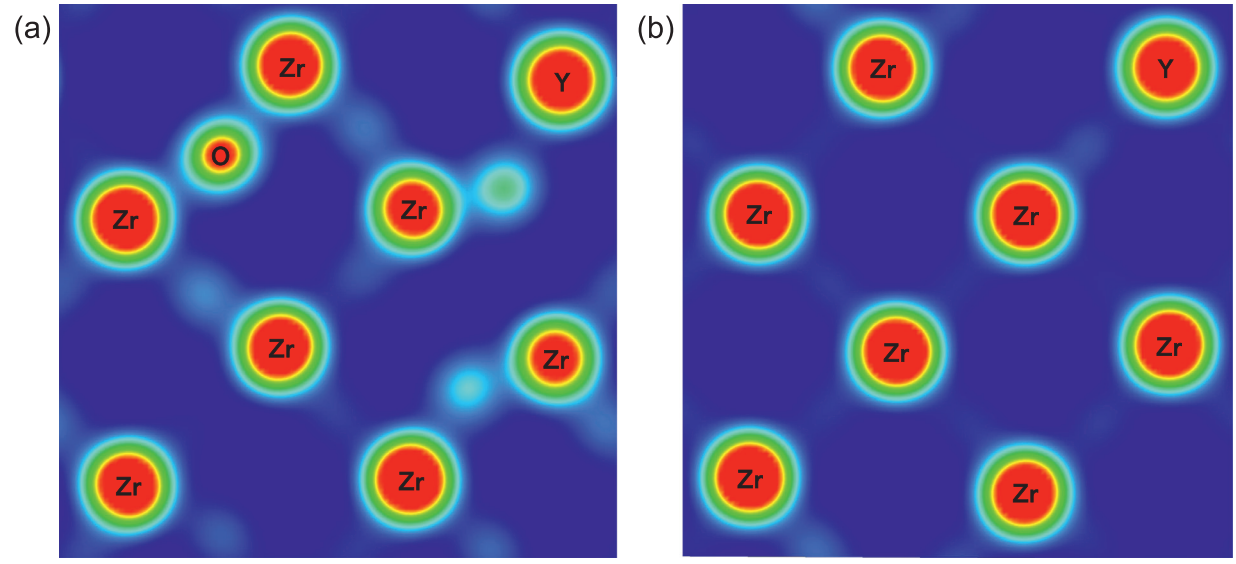

Fig. 5. 2D slice of charge density distributions for (100) planes across the cation layer (a) with and (b) without an intervening "special" O in a $Zr_{26}Y_6O_{62}$ supercell.

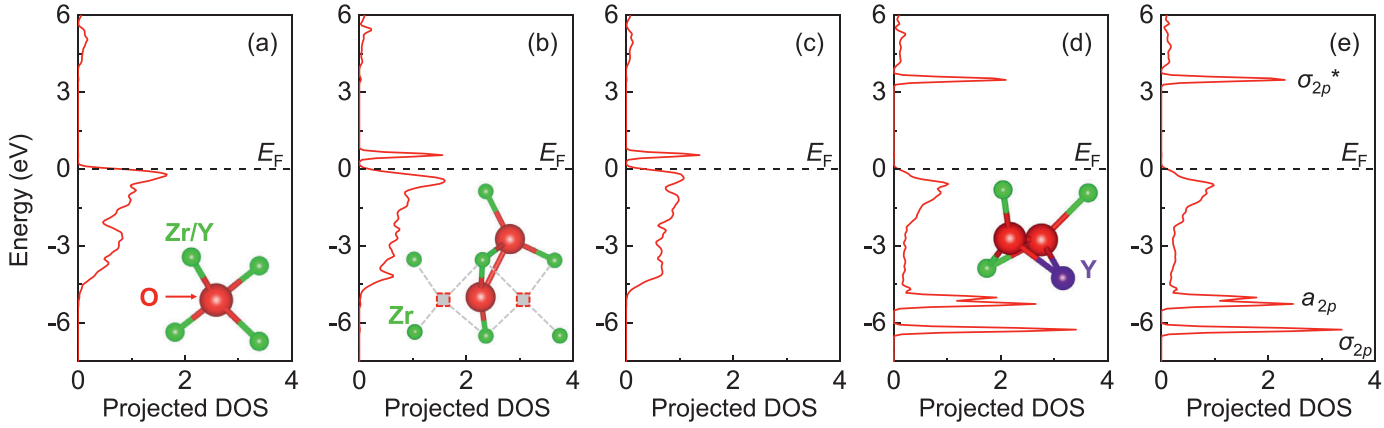

Fig. 6. Projected DOS of (a) O^{2-}, (b-c) two O in $(O_2)^{3-}$ complex, and (e-f) two O in $(O_2)^{2-}$ in a $Zr_{26}Y_6O_{63}$ supercell. Inset of (a): local structure of O^{2-}. Inset of (b): local structures of $(O_2)^{3-}$ complex whose projected DOS is shown in (b-c). Inset of (d): local structures of $(O_2)^{2-}$ whose projected DOS is shown in (d-e).

in the $Zr_{26}Y_6O_{62}$ supercell discussed above. (iii) There are spin-zero states below the conduction band minimum (CBM) at 3.50 eV and spin-zero states below the valence band at −6.26 eV, which as shall be explained, correspond to the anti-bonding orbital σ_{2p}* and the bonding orbital σ_{2p} of the peroxide group $(O_2)^{2-}$, respectively. When we analyzed the Bader charge and projected DOS of oxygen ions in the $Zr_{26}Y_6O_{63}$ supercell, three groups of O can be assigned to the above features. (i) Out of 63 O in total, 59 O have Bader charges of 7.30±0.02*e* that are slightly smaller than the Bader charges of O^{2-} in the $Zr_{26}Y_6O_{61}$ (7.31±0.03*e*) and $Zr_{26}Y_6O_{62}$ (7.31±0.02*e*) supercells calculated above. We found these are tetrahedral O (inset of Fig. 6a) and the projected DOS of one such O is shown in Fig. 6a, which is similar to that of O^{2-} in Fig. 4a except for a lowered E_F below VBM. These can be treated as O^{2-} with a delocalized hole state, which is responsible for the feature (i) in Fig. 3c. Even though individually the charge deficiency contribution is small (~0.01*e*), because of the numerous number of oxygen involved (59), this delocalized hole state occupies non-neglible weight in the total charge accounting for the supercell. (ii) Two O have Bader charges of 7.01*e* and 7.08*e*, respectively, and they form an O-O bond with a bond length of 2.43 Å. Regarding their local structures (inset of Fig. 6b), they are again displaced away from anion sublattice sites, with one O halfway between two neighboring Zr ions (enabled by an $V_O^{\bullet\bullet}$ in the neighboring anion site) and the other O in the center of a Zr-Zr-Y triangle (enabled by an $V_O^{\bullet\bullet}$ in the neighboring tetrahedral site). (The first O can also be viewed as sitting in the middle of two anion sublattice sites, which now become vacant as denoted by the shaded squares in the inset of Fig. 6b.) This local structure can be vividly seen by intervening O in the 2D slice of charge density distribution for a (100) plane cutting across the cation layer (Fig. 7a), which is more extreme than the case in Fig. 5a. Regarding the electronic structure, the projected DOS in Fig. 4b-4c shows that the two O share the unoccupied gap state peaked at 0.54 eV. Therefore, it can be similarly treated as $(O_2)^{3-}$ complex as discussed before, which is responsible for the feature (ii) in Fig. 3c. (iii) The remaining two O have Bader charges of 6.70*e* and 6.72*e*, respectively, and they form an O-O dimer with a very short bond length of 1.50 Å and a strong chemical bond (as indicated by the intense electron-cloud sharing in Fig. 7b, a 2D slice of charge density distribution for a (100) plane cutting across the oxygen layer). Regarding the local structure, the O-O dimer sits in the center of a Zr-Zr-Zr-Y tetrahedron (inset of Fig. 6d). A Bader charge accounting 6.71*e*−6*e*=0.71*e* would give 1.08*e* after the correction factor 1.53 ×, which is close to a formal charge assignment of α=1. These characteristics suggest a peroxide-group-like $(O_2)^{2-}$, which is further supported by the projected DOS in Fig. 6d-6e. Recall that for an isolated peroxide group $(O_2)^{2-}$, the molecular orbital theory describes an electron

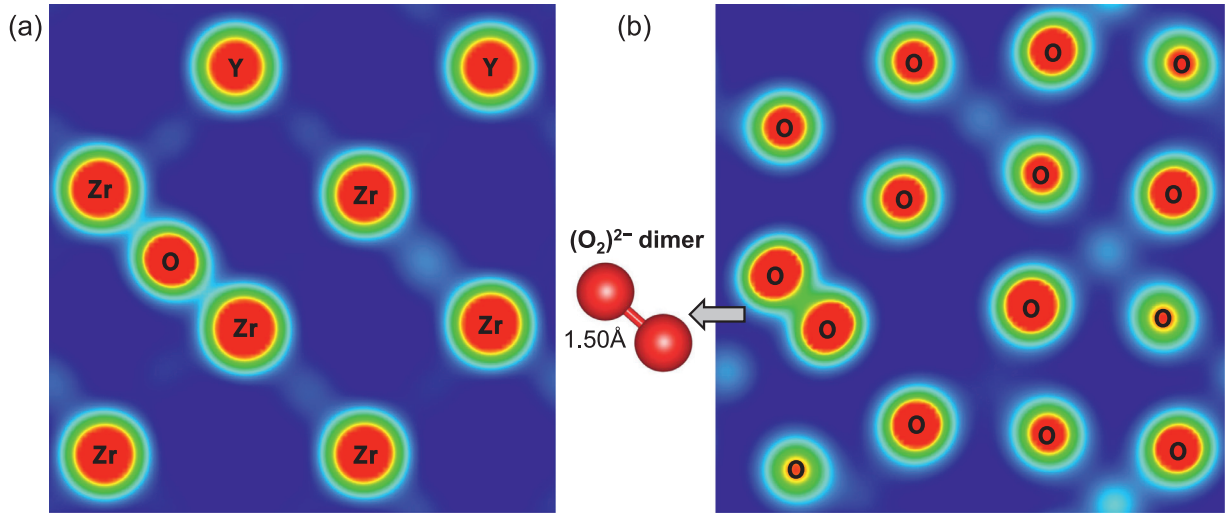

Fig. 7. 2D slice of charge density distributions for (100) planes (a) with an intervening O across the cation layer and (b) an O-O dimer across the oxygen layer in a $Zr_{26}Y_6O_{63}$ supercell.

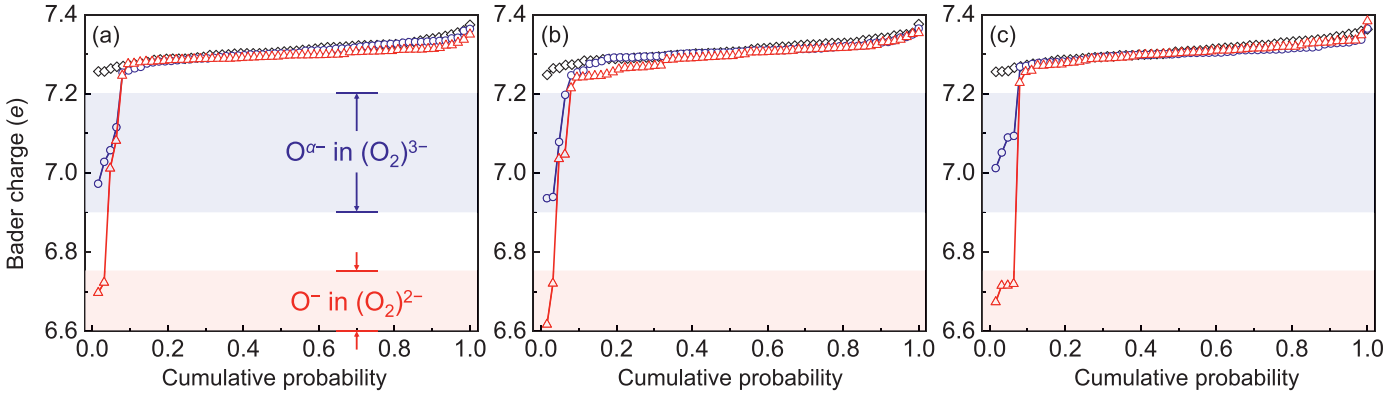

Fig. 8. (a-c) Three sets of Bader charge distributions for O in $Zr_{26}Y_6O_{61}$ (black diamond), $Zr_{26}Y_6O_{62}$ (blue cycle), and $Zr_{26}Y_6O_{63}$ (red triangle). Shaded regions in blue and in red are schematic energy ranges for $O^{\alpha-}$ and $(O_2)^{2-}$, respectively.

Table 1
Average values and standard deviations of Bader charges for three types of O in three sets of individually simulated $Zr_{26}Y_6O_{61}$, $Zr_{26}Y_6O_{62}$, and $Zr_{26}Y_6O_{63}$ supercells.

Set	Composition	Bader charge for O^{2-} (e)	Bader charge for $O^{\alpha-}$ in $(O_2)^{3-}$ (e)	Bader charge for O^- in $(O_2)^{2-}$ (e)
1	$Zr_{26}Y_6O_{61}$	7.31±0.03	/	/
	$Zr_{26}Y_6O_{62}$	7.31±0.02	7.04±0.06	/
	$Zr_{26}Y_6O_{63}$	7.30±0.02	7.05±0.05	6.71±0.02
2	$Zr_{26}Y_6O_{61}$	7.31±0.02	/	/
	$Zr_{26}Y_6O_{62}$	7.31±0.02	7.04±0.13	/
	$Zr_{26}Y_6O_{63}$	7.30±0.03	7.04±0.01	6.67±0.07
3	$Zr_{26}Y_6O_{61}$	7.31±0.03	/	/
	$Zr_{26}Y_6O_{62}$	7.30±0.02	7.06±0.04	/
	$Zr_{26}Y_6O_{63}$	7.30±0.02	/	6.71±0.02

configuration of $(\sigma_{2p})^2(\pi_{2p})^4(\pi_{2p}{}^*)^4(\sigma_{2p}{}^*)^0$. Using such information, in Fig. 6d-6e, the unoccupied states peaked at 3.50 eV can be treated as $\sigma_{2p}{}^*$, the occupied states peaked at −5.01 eV and −5.26 eV can be treated as π_{2p}, and the occupied states peaked at −6.26 eV can be treated as σ_{2p} for peroxide-group $(O_2)^{2-}$. Note in the crystal structure of cubic YSZ, the two π_{2p} orbitals are split under the tetrahedral field, and the $\pi_{2p}{}^*$ orbitals are strongly hybridized the Zr/Y 3*d* orbitals and become more distributed. Such peroxide-group-like $(O_2)^{2-}$ is responsible for the feature (iii) in Fig. 3c. As (i) the delocalized hole state has partially symmetric spin-up/down DOS, (ii) the $(O_2)^{3-}$ has one unpaired electron, and (iii) the $(O_2)^{2-}$ has zero unpaired electron, the simulated $Zr_{26}Y_6O_{63}$ supercell containing one delocalized hole state, one $(O_2)^{3-}$ complex and one $(O_2)^{2-}$ group has a net magnetic moment of $\mu_B<1.14\mu_B<2\mu_B$. Therefore, the three types of hole states in Fig. 3c can all be distinguished.

Lastly, we seek to justify the general applicability of the above findings by providing more examples. In Fig. 8a, we plotted the Bader charge distributions for O in the first set of simulated $Zr_{26}Y_6O_{61}$ (black diamond), $Zr_{26}Y_6O_{62}$ (blue cycle), and $Zr_{26}Y_6O_{63}$ (red triangle) supercells, whose atomic and electronic structures have been described above. Three types of O can be classified according to our discussions in the above: O^{2-} with Bader charge >7.2*e*, $O^{\alpha-}$ in $(O_2)^{3-}$ complex with Bader charge between 6.9*e* and 7.2*e*, and O^- in $(O_2)^{2-}$ group with Bader charge <6.75*e*. These classifications also apply to other two sets of individually simulated

$Zr_{26}Y_6O_{61}$, $Zr_{26}Y_6O_{62}$, and $Zr_{26}Y_6O_{63}$ supercells, as illustrated by the Bader charge distributions for O in Fig. 8b and 8c and detailed statistics summarized in Table 1. Interestingly, only $O^{\alpha-}$ in $(O_2)^{3-}$ complex can be observed in $Zr_{26}Y_6O_{62}$ (i.e., the "dilute" limit of our first-principles calculations), $(O_2)^{2-}$ group can always be observed $Zr_{26}Y_6O_{63}$, and the delocalized hole states are always accompanied with the formation of $(O_2)^{2-}$ group. Therefore, we conclude our results are general for YSZ with different atomic arrangements.

4. Discussions

Our results above have identified three types of hole states in oxidized YSZ, including (i) delocalized hole states, (ii) localized hole states on oxygen $O^{\alpha-}$ as part of $(O_2)^{3-}$ complex, with α=1.5, and (iii) peroxide-group-like $(O_2)^{2-}$, which have different implications on the functioning and stability of YSZ electrolytes. For (i), the band-like delocalized hole states mean greatly enhanced hole mobility/conductivity and a potential metal-insulator transition in over-oxidized YSZ, which if formed could enable novel applications as mixed ionic and electronic conductors, catalysts and memristors. (Over-oxidation of YSZ may be possible under large anodic polarizations, for example, in high-current-density SOEC and electrocatalysis.) Unfortunately, our simulation results found that the formation of delocalized hole states is always accompanied by the formation of peroxide-group-like $(O_2)^{2-}$, the latter of which competes with the former and leads to oxygen gas evolution and electrolyte degradation as shall be discussed. This is despite the fact that DFT method tends to over-delocalize electrons. Therefore, in real materials, the formation of peroxide-group-like $(O_2)^{2-}$ should be more favorable than the formation of delocalized hole states, which would pin the Fermi level at the top of oxygen 2*p* band and suppress the more conductive delocalized hole states in over-oxidized YSZ. Nevertheless, some exceptions may be possible at low temperatures, where the reaction kinetics of $(O_2)^{2-}$ disproportionation and oxygen gas evolution become sluggish.

For (ii), the localized hole states on oxygen $O^{\alpha-}$ suggest a small polaron mechanism, where a hole can be localized on two neighboring O for the $(O_2)^{3-}$ complex. It is consistent with the large activation energy of 1.05 eV for the hole mobility reported in 8YSZ at 800-1050°C. [4] As hole localization requires oxygen ions with extreme local structures and excessive lattice relaxation, hole migration is coupled with oxygen ion dynamics. This explains why the O^{2-} mobility has a smaller activation energy of 0.79 eV than that of the hole (both measured by the same study at the same temperature range [4]) in 8YSZ, because the former only requires an exchange between an $V_O^{\bullet\bullet}$ and a neighboring O^{2-} while the latter requires collective relaxation of multiple oxygen ions and $V_O^{\bullet\bullet}$. Indeed, the activation energy for the hole mobility is similar to that of O^{2-} at low temperatures <500°C, where O^{2-} movement becomes sluggish and collective with larger activation energy of 1.0-1.2 eV. [44,45] From this perspective, one may argue that a softer anion sublattice not only gives rise to higher $\sigma_{O^{2-}}$, but also higher σ_h because it offers many shallow energy traps for localized hole states with small migration barriers. This argument is supported by the conductivity data in YSZ (Fig. 1a) and another two fast O^{2-} conductors $Ce_{0.9}Gd_{0.1}O_{1.95-\delta}$ (GDC, Fig. 9a; it has a fluorite structure similar to YSZ) [46] and $La_{0.9}Sr_{0.1}Ga_{0.8}Mg_{0.2}O_{3-\delta}$ (LSGM, Fig. 9b; it has a perovskite structure) [47], and we note both $\sigma_{O^{2-}}$ and σ_h follow the same ranking of YSZ<GDC<LSGM at 800°C. In the literature, a similar argument has also been pointed out by West *et al.* [21,22]. They reported enhanced p-type conductivity in an oxidizing atmosphere and/or under a DC bias in acceptor-doped oxides with fluorite (YSZ) or perovskite structure $(Ba(Ti_{1-x}Ca_x)O_{3-x}$, $Sr(Ti_{1-x}Mg_x)O_{3-x}$, $Ca(Ti_{1-x}Mg_x)O_{3-x}$, and $(Bi_{1-x}Ca_x)FeO_{3-x/2})$ with defective anion sublattices, and proposed that the holes localize on "under-bonded O^{2-}" to form O^-. While being consistent with their proposal, our results suggest such under-bonded O^{2-} has a dynamic nature and the extreme local structure may only be created upon oxidization and may not exist in the ground-state un-oxidized structure. Furthermore, the under-bonded O^{2-} must form in pairs to achieve one effective hole localization, i.e., forming a $(O_2)^{3-}$ complex. Back to YSZ, our results identified that the hole states in oxidized YSZ are mainly constituted by $O^{\alpha-}$ (α=1.5) up to a composition of $Zr_{0.8125}Y_{0.1875}O_{1.9375}$ (i.e., $Zr_{26}Y_6O_{62}$). This corresponds to an over-stoichiometry of δ=0.03125 to the reference composition of $Zr_{0.8125}Y_{0.1875}O_{1.90625}$ (i.e., $Zr_{26}Y_6O_{61}$). Even though it is the most "dilute" situation for the simulated supercell, one should note that the defect concentration is already very high and may only be reached under a highly oxidizing condition. (While there are non-stoichiometric data available for reduced YSZ at low oxygen pressures [48], there are no such data reported for oxidized YSZ at high

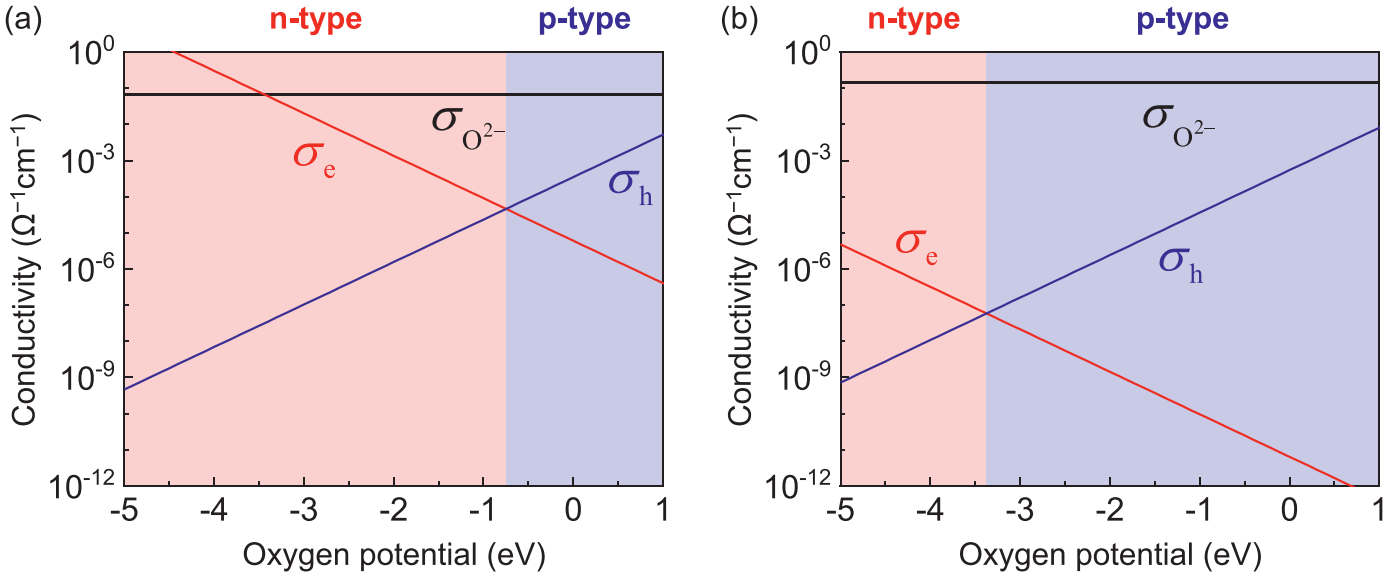

Fig. 9. Conductivity data of (a) GDC and (b) LSGM at 800°C. Shaded regions in red and blue denote the n- and p-type characteristics of the minor electronic conductivity, respectively.

oxygen pressures, which makes it difficult to quantify δ at a given condition at the present stage.) Lastly, because the localized hole states on oxygen $O^{\alpha-}$ form complexes with lattice oxygen ion as well as with $V_O^{\bullet\bullet}$, the migration of holes and oxygen ions/vacancies may again become correlated. It indicates a coupling between the ionic and electronic fluxes, especially under extremely oxidizing conditions. This possibility has been treated in Ref. [15], where O^- conduction is included to resolve the discrepancy between simulated and experimentally measured μ_{O_2} profiles in thick YSZ electrolytes.

For (iii), the peroxide-group-like $(O_2)^{2-}$ has been detected by Raman spectroscopy in YSZ powders treated in 30 vol% H_2O_2 solution at 5°C and dried at room temperature. [49] However, peroxide group is not stable and prone to disproportionation. Note our first-principles calculations were conducted as a closed system and the disproportionation reaction $2(O_2)^{2-} \rightarrow 2O^{2-} + O_2\uparrow$ with oxygen gas evolution was not treated. Therefore, in high-temperature applications of YSZ, the peroxide-group-like $(O_2)^{2-}$ once formed may react with more holes to generate oxygen bubbles, most likely at grain boundaries that are preferential sites for bubble nucleation and growth. The formation of oxygen bubbles has been observed in high-current-density SOEC both at the oxygen electrode/electrolyte interface and at the grain boundaries inside YSZ electrolyte, which leads to subsequent electrode delamination and electrolyte cracking. [3,18,50] To resolve such a problem, one should promote the formation and migration of (ii) the localized hole states on oxygen $O^{\alpha-}$ (α=1.5) inside the electrolyte before reaching the thermodynamic threshold to form $(O_2)^{2-}$. The enhanced σ_h also provides additional benefits to lower the electrode overpotential. Practically speaking, as σ_h is more challenging to measure and less are known, a high $\sigma_{O^{2-}}$ can be used as a descriptor to screen and select materials and dopants based on the $\sigma_{O^{2-}}$-σ_h-soft anion sublattice correlation discussed above. In fact, a buffering layer of GDC (which has higher $\sigma_{O^{2-}}$ and σ_h than YSZ) between YSZ electrolyte and oxygen electrode is known to suppress oxygen bubble formation, which agrees with our predictions. Yet it raises additional delamination problem at GDC/YSZ bi-layer interface. Therefore, we believe a single-phase YSZ electrolyte with a chemically engineered "soft" anion sublattice close to the oxygen electrode is a better approach to solve the problem.

Finally, we note that a hole can be effectively localized on an oxygen ion to form O^- in the lithium-excess cathode materials for lithium-ion batteries, while it requires two neighboring oxygen ions to form $(O_2)^{3-}$ complex in YSZ. This is because in the lithium-excess cathode materials, the cation sublattice contains two kinds of cations with dramatically different bonding states with the oxygen ions—Li with little hybridization and transition metal ions with strong hybridization. As a result, the fluctuations in local chemical compositions are able to render some oxygen ions with excess Li-O bonds even without much distortions on anion sublattice. More specifically, a Li-O-Li configuration for an octahedral O is effective to increase the energy of an O 2*p* orbital on top of the O 2*p* band and realizes a localized hole. In contrast, in YSZ, Zr and Y have similar bonding states with the oxygen ions, so there are no fluctuations in local chemical compositions of oxygen ions so to speak. Accordingly, the degenerate O 2*p* orbital can only be realized by displacing oxygen ions from their lattice sites, and even so, the relaxations are insufficient to achieve one hole localization per oxygen ion. Instead, the underbonded oxygen ions must be formed in pairs to successfully localize one hole, namely an $(O_2)^{3-}$ complex discussed above. To approach a situation similar to that in the lithium-excess cathode materials, main-group dopants such as Ca and Mg can be used to replace Y in YSZ, which may result in better hole localization as well as a decoupling in the anion-hole dynamics.

5. Conclusions

(1) The chemical and structural natures of hole states in oxidized YSZ have been simulated by first-principles calculations and analyzed. Three types of hole states with distinct local structural features have been identified, including delocalized hole states, localized hole states on oxygen $O^{\alpha-}$ (α=1.5) and peroxide-group-like $(O_2)^{2-}$.

(2) The delocalized hole states are shared by tetrahedral-site oxygen ion O^{2-} with Bader charges >7.2*e*. In the electronic structure, the Fermi level E_F enters the top of the conduction band. The band-like feature suggests greatly enhanced hole mobility and conductivity and a potential metal-insulator transition for YSZ under highly oxidizing conditions. However, its formation may be suppressed in real applications by the competing mechanism of forming $(O_2)^{2-}$ and generating oxygen gas.

(3) The localized hole states on oxygen $O^{\alpha-}$ form $(O_2)^{3-}$ complexes with Bader charge between 6.9*e* and 7.2*e* per oxygen, involving under-bonded oxygen ions in pairs that are severely displaced away from the lattice sites as well as a neighboring oxygen vacancy. The localized hole state has an energy level slightly above the VBM and follows a small polaron mechanism.

(4) The peroxide-group-like $(O_2)^{2-}$ contains chemically bonded O-O dimer with a short bond distance of ~1.5 Å, with Bader charge <6.75*e*. Its electronic structure is similar to that of an isolated peroxide group $(O_2)^{2-}$, with fully occupied σ_{2p}, π_{2p} and $\pi_{2p}{}^*$ orbitals and an empty $\sigma_{2p}{}^*$ orbital.

(5) In the dilute limit, the localized hole states on oxygen $O^{\alpha-}$ with α=1.5 ($(O_2)^{3-}$ complexes) dominate in oxidized YSZ, which is responsible for the experimentally observed thermally activated hole conductivity. Its concentration and correspondingly the hole conductivity can be enhanced under low PO_2 atmosphere and/or anodic polarization. Under more extreme oxidizing conditions, the formation of the peroxide-group-like $(O_2)^{2-}$ could take over and its disproportionation reaction is related to the formation of oxygen bubbles at YSZ grain boundaries in high-current-density operation and/or long-time service of SOEC. The formation of $(O_2)^{2-}$ and subsequent disproportionation and oxygen gas evolution may also pin the Fermi level on top of the O 2*p* band and suppress the more conductive delocalized hole state to form in YSZ.

(6) The hole localization in YSZ relies on relaxations of anion sublattice, which couples the dynamics of oxygen ions and holes. A "softer" anion sublattice is expected to enhance both $\sigma_{O^{2-}}$ and σ_h, which could help to mitigate electrolyte degradations in SOEC operations.

Declaration of Competing Interest

The authors declare that they have no known competing financial interests or personal relationships that could have appeared to influence the work reported in this paper.

Acknowledgement

We acknowledge support by the Department of Energy, Basic Energy Sciences, under award number DE-SC0002633 (Chemomechanics of Far-From-Equilibrium Interfaces), and the U.S. Department of Energy (USDOE), Office of Energy Efficiency and Renewable Energy (EERE), Advanced Manufacturing Office (AMO) R&D Projects Emerging Research Exploration, under DOE Idaho Operations Office with contract no. DE-AC07-05ID14517.

References

[1] D.R. Clarke, C.G. Levi, Materials design for the next generation thermal barrier coatings, Annu. Rev. Mater. Res. 33 (2003) 383–417.

[2] S. Park, J.M. Vohs, R.J. Gorte, Direct oxidation of hydrocarbons in a solid-oxide fuel cell, Nature 404 (2000) 265–267.
[3] C. Graves, S.D. Ebbesen, S.H. Jensen, S.B. Simonsen, M.B. Mogensen, Eliminating degradation in solid oxide electrochemical cells by reversible operation, Nature Mater 14 (2015) 239–244.
[4] J.-H. Park, R.N. Blumenthal, Electronic transport in 8 mole percent Y_2O_3-ZrO_2, J. Electrochem. Soc. 136 (1989) 2867–2876.
[5] L. Zhang, L. Zhu, A.V. Virkar, Electronic conductivity measurement of yttria-stabilized zirconia solid electrolytes by a transient technique, J. Power Sources 302 (2016) 98–106.
[6] L. Zhu, L. Zhang, A.V. Virkar, Measurement of ionic and electronic conductivities of yttria-stabilized zirconia by an embedded electrode method, J. Electrochem. Soc. 162 (2015) F298–F309.
[7] Y. Dong, I.W. Chen, Mobility transition at grain boundaries in two-step sintered 8 mol% yttria-stabilized zirconia, J. Am. Ceram. Soc. 101 (2018) 1857–1869.
[8] Y. Dong, L. Qi, J. Li, I.W. Chen, A computational study of yttria-stabilized zirconia: II. Cation diffusion, Acta Mater 126 (2017) 438–450.
[9] Y. Dong, H. Yang, L. Zhang, X. Li, D. Ding, X. Wang, J. Li, J. Li, I.W. Chen, Ultra-uniform nanocrystalline materials via two-step sintering, Adv. Funct. Mater. 2007750 (2020), doi:10.1002/adfm.202007750.
[10] M. Kilo, C. Argirusis, G. Borchardt, R.A. Jackson, Oxygen diffusion in yttria stabilised zirconia—experimental results and molecular dynamics calculations, Phys. Chem. Chem. Phys. 5 (2003) 2219–2224.
[11] R. Pornprasertsuk, P. Ramanarayanan, C.B. Musgrave, F.B. Prinz, Predicting ionic conductivity of solid oxide fuel cell electrolyte from first principles, J. Appl. Phys. 98 (2005) 103513.
[12] A. Kushima, B. Yildiz, Oxygen ion diffusivity in strained yttria stabilized zirconia: Where is the fastest strain? J. Mater. Chem. 20 (2010) 4809–4819.
[13] A.V. Virkar, Theoretical analysis of the role of interfaces in transport through oxygen ion and electron conducting membranes, J. Power. Sources 147 (2005) 8–31.
[14] T. Jacobsen, M. Mogensen, The course of oxygen partial pressure and electric potentials across an oxide electrolyte cell, ECS Trans 13 (2008) 259–273.
[15] Y. Dong, I.W. Chen, Oxygen potential transition in mixed conducting oxide electrolyte, Acta Mater 156 (2018) 399–410.
[16] Y. Dong, Z. Zhang, A. Alvarez, I.W. Chen, Potential jumps at transport bottlenecks cause instability of nominally ionic solid electrolytes in electrochemical cells, Acta Mater 199 (2020) 264–277.
[17] C. Chatzichristodoulou, M. Chen, P.V. Hendriksen, T. Jacobsen, M.B. Mogensen, Understanding degradation of solid oxide electrolysis cells through modeling of electrochemical potential profiles, Electrochim. Acta 189 (2016) 265–282.
[18] B.-Y. Park, Q. Zhang, P.W. Voorhees, S.A. Barnett, Conditions for stable operation of solid oxide electrolysis cells: Oxygen electrode effects, Energy Environ. Sci. 12 (2019) 3053–3602.
[19] L. Zhang, L. Zhu, A.V. Virkar, Modeling of oxygen chemical potential distribution in solid oxide electrolyzer cells, J. Electrochem. Soc. 166 (2019) F1275–F1283.
[20] A. Alvarez, Y. Dong, I.W. Chen, DC electrical degradation of YSZ: Voltage-controlled electrical metallization of a fast ion conducting insulator, J. Am. Ceram. Soc. 103 (2020) 3178–3193.
[21] N. Maso, A.R. West, Electronic conductivity in yttria-stabilized zirconia under a small *dc* bias, Chem. Mater. 27 (2015) 1552–1558.
[22] X. Vendrell, A.R. West, Induced *p*-type semiconductivity in yttria-stabilized zirconia, J. Am. Ceram. Soc. 102 (2019) 6100–6106.
[23] M. Jovani, H. Beltran-Mir, E. Cordoncillo, A.R. West, Field-induced *p*-*n* transition in yttria-stabilized zirconia, Sci. Rep. 9 (2019) 18538.
[24] Y. Dong, H. Wang, I.W. Chen, Electrical and hydrogen reduction enhances kinetics in doped zirconia and ceria: I. Grain growth study, J. Am. Ceram. Soc. 100 (2017) 876–886.
[25] Y. Dong, I.W. Chen, Electrical and hydrogen reduction enhances kinetics in doped zirconia and ceria: II. Mapping electrode polarization and vacancy condensation in YSZ, J. Am. Ceram. Soc. 101 (2018) 1058–1073.
[26] Y. Dong, L. Qi, J. Li, I.W. Chen, Electron localization enhances cation diffusion in transition metal oxides: An electronic trebuchet effect, arXiv:1808.05196.
[27] M. Cologna, B. Rashkova, R. Raj, Flash sintering of nanograin zirconia in <5 s at 850°C, J. Am. Ceram. Soc. 93 (2010) 3556–3559.
[28] R. Kirchheim, On the mixed ionic and electronic conductivity in polarized yttria stabilized zirconia, Solid State Ionics 320 (2018) 239–258.
[29] H. Yoshida, Y. Sasaki, Low temperature and high strain rate superplastic flow in structural ceramics induced by strong electric-field, Scripta Mater 146 (2018) 173–177.
[30] J.S. Thorp, A. Aypar, J.S. Ross, Electron spin resonance in single crystal yttria stabilized zirconia, J. Mater. Sci. 7 (1972) 729–734.
[31] R.E.W. Casselton, Blackening in yttria stabilized zirconia due to cathodic processes at solid platinum electrodes, J. Appl. Electrochem. 4 (1974) 25–48.
[32] K.-H. Xue, P. Blaise, L.R.C. Fonseca, Y. Nishi, Prediction of semimetallic tetragonal Hf_2O_3 and Zr_2O_3 from first principles, Phys. Rev. Lett. 110 (2013) 065502.
[33] G. Assat, J.-M. Tarascon, Fundamental understanding and practical challenges of anionic redox activity in Li-ion batteries, Nature Energy 3 (2018) 373–386.
[34] Z. Zhu, D. Yu, Y. Yang, C. Su, Y. Huang, Y. Dong, I. Waluyo, B. Wang, A. Hunt, X. Yao, J. Lee, W. Xue, J. Li, Gradient Li-rich oxide cathode particles immunized against oxygen release by a molten salt treatment, Nature Energy 4 (2019) 1049–1058.
[35] K. Luo, M.R. Roberts, R. Hao, N. Guerrini, D.M. Pickup, Y.-S. Liu, K. Edstrom, J. Guo, A.V. Chadwick, L.C. Duda, P.G. Bruce, Charge-compensation in 3*d*-transition-metal-oxide intercalation cathodes through the generation of localized electron holes on oxygen, Nature Chem 8 (2016) 684–691.
[36] D.-H. Seo, J. Lee, A. Urban, R. Malik, S.Y. Kang, G. Ceder, The structural and chemical origin of the oxygen redox activity in layered and cation-disordered Li-excess cathode materials, Nature Chem 8 (2016) 692–697.
[37] G. Kresse, D. Joubert, From ultrasoft pseudopotentials to the projector augmented-wave method, Phys. Rev. B 59 (1999) 1758.
[38] G. Kresse, J. Furthmüller, Efficiency of ab-initio total energy calculations for metals and semiconductors using a plane-wave basis set, Comput. Mater. Sci. 6 (1996) 15–50.
[39] J.P. Perdew, K. Burke, M. Ernzerhof, Generalized gradient approximation made simple, Phys. Rev. Lett. 77 (1996) 3865–3868.
[40] C.R.A. Catlow, A.C. Chadwick, G.N. Greaves, L.M. Moroney, EXAFS study of yttria-stabilized zirconia, J. Am. Ceram. Soc. 69 (1986) 272–277.
[41] Y. Dong, L. Qi, J. Li, I.W. Chen, A computational study of yttria-stabilized zirconia: I. Using crystal chemistry to search for the ground state on a glassy energy landscape, Acta Mater 127 (2017) 73–84.
[42] K. Momma, F. Izumi, VESTA 3 for three-dimensional visualization of crystal, volumetric and morphology data, J. Appl. Crystallogr. 44 (2011) 1272–1276.
[43] W. Tang, E. Sanville, G. Henkelman, A grid-based Bader analysis algorithm without lattice bias, J. Phys.: Condens. Matter 21 (2009) 084204.
[44] K.L. Ngai, Evidence of interaction between oxygen ions from conductivity relaxation and quasielastic light scattering data of yttria-stabilized zirconia, Philos. Mag. B 77 (1998) 187–195.
[45] Y. Li, J. Gong, Y. Xie, Y. Chen, Analysis of non-linear Arrhenius behavior of ionic conduction in cubic zirconia stabilized with yttria and calcia, J. Mater. Sci. Lett. 21 (2002) 157–159.
[46] C. Chatzichristodoulou, P.V. Hendriksen, Electronic conductivity of $Ce_{0.9}Gd_{0.1}O_{1.95-\delta}$ and $Ce_{0.8}Pr_{0.2}O_{2-\delta}$: Hebb-Wagner polarisation in the case of redox active dopants and interface, Phys. Chem. Chem. Phys. 13 (2011) 21558–21572.
[47] J.-H. Kim, H.-I. Yoo, Partial electronic conductivity and electrolytic domain of $La_{0.9}Sr_{0.1}Ga_{0.8}Mg_{0.2}O_{3-\delta}$, Solid State Ionics 140 (2001) 105–113.
[48] J.-H. Park, R.N. Blumenthal, Thermodynamic properties of nonstoichiometric yttria-stabilized zirconia at low oxygen pressures, J. Am. Ceram. Soc. 72 (1989) 1485–1487.
[49] S.C. Middleburgh, I. Ipatova, L.J. Evitts, M.J.D. Rushton, B. Assinder, R.W. Grimes, W.E. Lee, Evidence of excess oxygen accommodation in yttria partially-stabilized zirconia, Scripta Mater 175 (2020) 7–10.
[50] M.A. Laguna-Bercero, R. Campana, A. Larrea, J.A. Kilner, V.M. Orera, Electrolyte degradation in anode supported microtubular yttria stabilized zirconia-based solid oxide steam electrolysis cells at high voltages of operation, J. Power Sources 196 (2011) 8942–8947.